Journal of Solid State Chemistry 181 (2008) 3269–3277

Contents lists available at ScienceDirect

Journal of Solid State Chemistry

journal homepage: www.elsevier.com/locate/jssc

Synthesis, magnetism and electronic structure of $YbNi_{2-x}Fe_xAl_8$ ($x = 0.91$) isolated from Al flux

Xiuni Wu [a], Melanie Francisco [d], Zsolt Rak [b], T. Bakas [c], S.D. Mahanti [b], Mercouri G. Kanatzidis [d,*]

[a] Department of Physical Sciences, Rhode Island College, Providence, RI 02908, USA
[b] Department of Physics, Michigan State University, East Lansing, MI 48824, USA
[c] Department of Physics, University of Ioannina, GR-45110 Ioannina, Greece
[d] Department of Chemistry, Northwestern University, Evanston, IL 60208, USA

ARTICLE INFO

Article history:
Received 7 June 2008
Received in revised form
22 August 2008
Accepted 26 August 2008
Available online 13 September 2008

Keywords:
Intermetallics
Flux synthesis
Band calculations

ABSTRACT

The combination of ytterbium, nickel, iron in liquid aluminum resulted in the formation of the new intermetallic compound $YbNi_{2-x}Fe_xAl_8$ ($x = 0.91$) which adopts the $CaCo_2Al_8$ structure type with $a = 14.458(3)$ Å, $b = 12.455(3)$ Å, $c = 3.9818(8)$ Å and space group *Pbam*. Its resistivity drops with decreasing temperature, saturating to a constant value at lower temperatures. Above 50 K, the inverse magnetic susceptibility data follows Curie–Weiss Law, with a calculated $\mu_{eff} = 2.19\,\mu_B$. Although the observed reduced moment in magnetic susceptibility measurement suggests that the Yb ions in this compound are of mixed-valent nature, *ab initio* electronic structure calculations within density functional theory using LDA+*U* approximation give an f^{13} configuration in the ground state.

1. Introduction

Complex rare-earth aluminides are a growing class of intermetallics that has been identified predominantly through the application of metallic fluxes as a synthetic tool. Yb-based intermetallics display a variety of interesting physical properties such as mixed valency [1], super conductivity, heavy fermion [2] and Kondo-lattice behavior [3]. These characteristics are associated with the fact that the $4f^{13}$ and $4f^{14}$ electronic configurations of Yb are close in energy and they hybridize easily with the conduction electrons. In this sense, Yb is often considered as a $4f^{13}$ hole-analog to the Ce $4f^1$ electronic configuration. Ce-based intermetallic materials are more extensively studied, possibly because of the difficulty in synthesizing pure samples of Yb-based compounds associated with the high vapor pressure of Yb [4]. Ytterbium analogs have been successfully synthesized in the $RETM_2Tr_8$ system (*RE* = rare earth, *TM* = transition metal, *Tr* = Al, Ga and In), along with Ce and Pr [5,6]. These compounds adopt the so-called $CaCo_2Al_8$ structure type. $CeFe_2Al_8$ is a rare example of a valence fluctuation compound containing Fe [7]. Mössbauer spectra indicate that the Fe atoms in $CeFe_2Al_8$ do not carry any magnetic moment [8]. $PrCo_2Al_8$ orders antiferromagnetically at 5 K, with a clear metamagnetic transition occurring at a critical field of 9000 G [9]. Several gallides adopting the $CaCo_2Al_8$ structure have also been reported, namely $REFe_2Ga_8$ (*RE* = Ce, Pr, Nd, Sm) [10], $RECo_2Ga_8$ (*RE* = Ce, Pr, Eu, Yb) [10,11] and $RERu_2Ga_8$ (*RE* = La, Ce, Pr, Nd) [12], whereas $EuRh_2In_8$ was the first indide analog of this structure type [13].

The problem of high vapor pressure of ytterbium at high temperatures can be mitigated using flux synthesis, which is an effective method in exploring new material and obtaining high-quality single crystals [14]. Given the existence of $YbCo_2Al_8$ we explored the Yb–Ni–Fe–Al composition where the combination of Ni and Fe would be isoelectronic to two Co atoms. This led to the isostructural compound $YbNi_{2-x}Fe_xAl_8$ ($x = 0.91$), which appears to be the first quaternary example reported in the $RETM_2Tr_8$ family.

Herein we describe the synthesis, crystal structure, physical properties and ^{57}Fe Mössbauer spectroscopy measurements of $YbNi_{2-x}Fe_xAl_8$ ($x = 0.91$). In addition, we present detailed electronic structure calculations using *ab initio* density functional methods allowing for strong intra-site Coulomb repulsion for the *f* electrons giving rise to an f^{13} Yb^{3+} system [15–18].

2. Experimental section

2.1. Reagents

The following reagents were used as obtained: ytterbium (Cerac, 99.9%), nickel (99%, 325 mesh, Sargent, Buffalo Grove, IL),

* Corresponding author.
E-mail address: m-kanatzidis@northwestern.edu (M.G. Kanatzidis).

0022-4596/$ - see front matter © 2008 Elsevier Inc. All rights reserved.
doi:10.1016/j.jssc.2008.08.029

iron (99.99%, fine powder, Aldrich Chemical, Milwaukee, WI), aluminum (Cerac, 99.5%, −20 mesh).

2.2. Synthesis

Yb, Ni and Fe were mixed with excess Al in a nitrogen-filled glove-box. Alumina crucibles containing a mixture of 1 mmol of Yb metal (0.173 g), 1 mmol of Ni (0.059 g), 1 mmol of Fe (0.056 g) and 10 mmol of Al (0.270 g) were placed into silica tubes (13 mm o.d.), which were then sealed under vacuum ($\sim 10^{-4}$ Torr). The samples were heated to 1000 °C in 15 h, maintained at this temperature for 5 h, and cooled to 850 °C in 2 h. The mixtures were then annealed at 850 °C for 3 days, cooled to 500 °C in 35 h, and finally to room temperature in 10 h.

The excess aluminum was removed by soaking the crucible in aqueous 5 M NaOH solution overnight. The remaining crystalline product was rinsed with water and acetone. The major phase in the product was determined to be $YbNi_{2-x}Fe_xAl_8$ with a yield of 70–90%; while a small amount of $Yb_3Ni_5Al_{19}$ was also observed [19].

2.3. Scanning electron microscopy and elemental analysis

The crystals were selected and placed on a scanning electron microscope (SEM) sample plate using carbon tape. The chemical compositions of the products were determined by energy dispersive spectroscopy (EDS) performed on a JEOL JSM-35C SEM equipped with a NORAN EDS detector. Data were acquired by applying a 25 kV accelerating voltage with an accumulation time of 40 s. Typical crystals of $YbNi_{2-x}Fe_xAl_8$ feature needle morphologies as shown in Fig. 1. Over 20 crystals were analyzed with the resulting average elemental composition corresponding to the ratio of 1:1:1:8.

2.4. X-ray crystallography

Single-crystal X-ray diffraction data were collected for $YbNi_{2-x}Fe_xAl_8$ at room temperature on a Bruker AXS SMART CCD X-ray diffractometer. A data collection (Mo$K\alpha$ radiation, $\lambda = 0.71073$ Å) was acquired covering a full sphere of reciprocal space using exposure time 20 s/frame. The data acquisition and cell reduction were done with the SMART [20] software package and data processing was performed with the SAINTPLUS program [21]. An empirical absorption correction was applied to the data using the SADABS program [22]. The structure was solved using direct methods and refined with the SHELXTL package program [23]. Systematic absence conditions led to two possible space groups: *Pbam* and *Pba*2. The mean value of $|E^2-1|$ was 0.969 indicating that the structure was likely centrosymmetric. The centrosymmetric space group has a much lower combined figure of merit (CFOM) value and was found to be correct after final refinement.

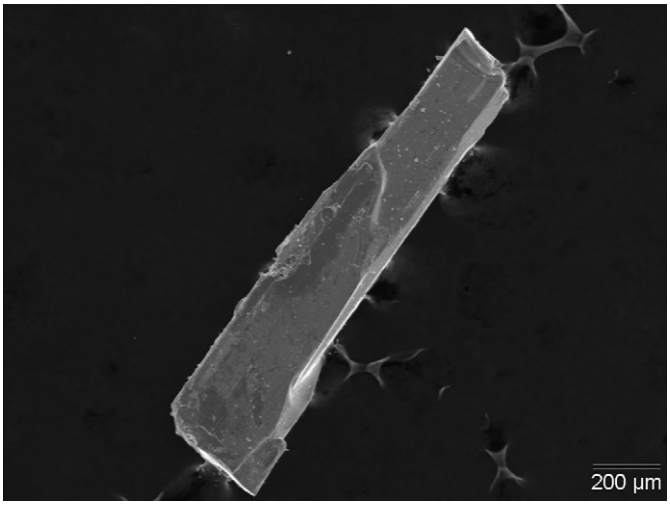

Fig. 1. SEM image of a typical crystal of $YbNi_{2-x}Fe_xAl_8$ grown from aluminum flux.

In the structure of $YbNi_{2-x}Fe_xAl_8$, a total of 12 atomic sites including one Yb, two transition metal sites (Ni/Fe) and nine Al sites were identified. Originally the data was collected at 173 K covering a hemisphere of reciprocal space. Since the atomic numbers of Ni and Fe are very close to each other, different assignments on these two transition metal sites $M(1)$ and $M(2)$ were examined. Two satisfactory solutions were obtained: (a) the $M(1)$ site was occupied by Ni and the $M(2)$ was occupied by Fe with both sites fully occupied; (b) both M sites were occupied by a mixture of Ni/Fe: for $M(1)$, Ni and Fe were found to have an occupation of 84.6% and 15.4%, respectively; while for $M(2)$, the corresponding values were 33.5% and 66.5%. To further check this assignment, we collected single-crystal X-ray data covering a full sphere of reciprocal space. It was found that when the $M(1)$ site was assigned to Ni and the $M(2)$ site to Fe, the occupancy factors were 0.95 and 1.03, respectively, R_1 and wR_2 were 2.61% and 5.72%. If these two sites were switched, the occupancy factors were 1.06 and 0.94, R_1 and wR_2 values were 2.51% and 5.77%. As a result, the $M(1)$ and $M(2)$ sites were refined as mixed occupancy of Ni and Fe: 63%/37% on $M(1)$ and 46%/54% on $M(2)$ for Ni/Fe. This refinement gave the R values with R_1 2.52% and wR_2 3.95%. The resulting stoichiometry is in agreement with the elemental analysis from EDS. Data collection parameters and refinement details for $YbNi_{2-x}Fe_xAl_8$ are shown in Table 1. Atomic positions and occupancies are listed in Table 2.

The X-ray powder diffraction data were collected at room temperature on a CPS 120 INEL X-ray diffractometer (Cu$K\alpha$) equipped with position-sensitive detector. Experimental powder patterns were compared to the patterns calculated from the single-crystal structure solution (by the CrystalDiffract program [24]) to assess phase identity and purity.

Table 1
Selected crystal data and structure refinement details for $YbNi_{2-x}Fe_xAl_8$

Empirical formula	$YbNi_{2-x}Fe_xAl_8$
Formula weight	503.44
Crystal system	Orthorhombic
Space group	*Pbam* (#55)
Unit cell dimensions	$a = 14.458(3)$ Å
	$b = 12.455(3)$ Å
	$c = 3.9818(8)$ Å
Volume	717.1(2) Å^3
Z	4
Density (calculated)	4.663 Mg/m^3
Absorption coefficient	18.404 mm^{-1}
$F(000)$	912
Crystal size	$0.22 \times 0.30 \times 0.24$ mm^3
θ range for data collection	2.82–27.79°
Limiting indices	$-16 \leqslant h \leqslant 16$
	$-19 \leqslant k \leqslant 18$
	$-5 \leqslant l \leqslant 5$
Reflections collected	6852
Independent reflections	929 [$R_{int} = 0.0275$]
Completeness to $\theta = 37.00°$	95.6%
Data/restraints/parameters	929/0/72
Goodness-of-fit on F^2	1.056
Final R indices [$I > 2\sigma(I)$]	$R_1 = 0.0252$, w$R_2 = 0.1041$
R indices (all data)	$R_1 = 0.0259$, w$R_2 = 0.1052$
Largest diff. peak and hole	2.316 and −1.497 e Å^{-3}

$R_1 = \sum(|F_o| - |F_c|) / \sum |F_o|$; $wR_2 = \left\{\sum\left[w(F_o^2 - F_c^2)\right] / \left[\sum (w|F_o|^2)^2\right]\right\}^{1/2}$.

Table 2
Atomic coordinates ($Å \times 10^4$) and occupancies ($Å^2 \times 10^3$) for $YbNi_{2-x}Fe_xAl_8$

Atom	*Wyk* symbol	*x*	*y*	*z*	Occu.
Yb	4*h*	1579(1)	1809(1)	5000	1.0
Ni(1)	4*h*	342(1)	4075(1)	5000	0.63
Fe(1)	4*h*	342(1)	4075(1)	5000	0.37
Ni(2)	4*h*	1509(1)	977(1)	5000	0.46
Fe(2)	4*h*	1509(1)	977(1)	5000	0.54
Al(1)	2*a*	0	0	5000	1.0
Al(2)	4*g*	3374(2)	8788(2)	0	1.0
Al(3)	4*g*	2634(2)	6748(1)	0	1.0
Al(4)	4*h*	977(1)	2547(1)	5000	1.0
Al(5)	4*g*	−247(2)	8668(1)	0	1.0
Al(6)	4*g*	1680(2)	9912(2)	0	1.0
Al(7)	4*g*	482(2)	6812(1)	0	1.0
Al(8)	2*d*	0	5000	0	1.0
Al(9)	4*h*	1626(2)	5453(2)	5000	1.0

U_{eq} is defined as one -third of the trace of the orthogonalized U_{ij} tensor.

2.5. Physical properties characterization

Magnetic measurements were carried out on single crystals and polycrystalline samples of $YbNi_{2-x}Fe_xAl_8$. Field cooled and zero-field cooled dc magnetization measurements were performed for the above samples using a Quantum Design MPMS SQUID magnetometer. EDS-analyzed crystals were ground into powder, which was sealed in Kapton tape and placed into the magnetometer. Data were also collected from intact single crystals and the magnetic moments obtained agreed well with those of the ground polycrystalline samples. The data were collected in the temperature range of 3–300 K at 1000 G, while field-dependent magnetic measurements, conducted at 5 K, were carried out in fields up to ±55,000 G. A diamagnetic correction was applied to the data to account for the core diamagnetism.

Electrical resistivity was measured over the temperature range of 5–300 K using a four-probe dc technique with contacts made by silver paste on a pressed-pellet sample of $YbNi_{2-x}Fe_xAl_8$. Single crystals of $YbNi_{2-x}Fe_xAl_8$ were selected, ground into powder and pressed into a pellet of 3 mm length, 2 mm width and 0.2 mm thickness. The pellet sample was annealed at 350 °C for 3 h. Thermopower data were collected on the pellet of $YbNi_{2-x}Fe_xAl_8$ from 300 to 400 K with an MMR Technologies Inc. Seebeck measurement system.

Heat capacity measurements were collected on 6.8 mg of $YbNi_{2-x}Fe_xAl_8$ single crystals. Data were taken on a Quantum Design Physical Properties Measurement System (PPMS) in the temperature range 1.9–300 K in zero magnetic fields. Low-temperature grease provided by the instrument manufacturer was used to ensure good contact between the sample and sample holder.

The Mössbauer spectra were taken on polycrystalline sample of $YbNi_{2-x}Fe_xAl_8$ with a constant-acceleration spectrometer equipped with a ^{57}Co source in Rh matrix. The spectrometer was calibrated with metallic iron, and the isomer shift values are reported relative to α-Fe. A closed-loop refrigerator system was used for the low-temperature measurements. An Oxford Instrument Variox 316 cryostat was used for measurements at liquid-helium temperature.

2.6. Electronic structure calculations

Ab initio electronic structure calculations were performed using all-electron self-consistent full potential linearized augmented plane wave method (FP-LAPW) [25] within density functional theory (DFT) [15,16] as implemented in the WIEN2k program [26]. The exchange and correlation potential was incorporated through the local spin density approximation (LSDA) [27], necessary for magnetic systems. In order to overcome the inability of DFT to accurately model the ground state of systems containing rare-earth and/or transition metal atoms, the LSDA+*U* [17] formalism was used with the "around the mean field" (AMF) [18] setup. In this method the orbital-dependent Coulomb potential is only taken into account for the localized *f*- and *d*-states, while the delocalized (*s* and *p*) states are treated by orbital-independent LSDA-type potential. For $YbNi_{2-x}Fe_xAl_8$ the on-site Coulomb repulsion parameter *U* of the LSDA+*U* method was chosen to be $U(Yb) = 0.6$ Ry (8.04 eV) for the Yb *f*-states and $U(Ni) = U(Fe) = 0.4$ Ry (5.36 eV) for the Ni and Fe *d*-states. These values of *U* are taken from the literature [28,29], which are physically reasonable. The calculations were performed with the following setup: The muffin–tin radii values (in atomic units; 1 au = 0.529 Å) were chosen as 2.5 for Yb, 2.33 for Ni and Fe and 2.07 for all the Al atoms, the cutoff parameter was $RK_{max} = 7$, and the energy separation between the valence and the core states was −6.0 Ry. Self-consistent iterations were performed with 12*k* points in the irreducible part of the Brillouin zone (IBZ), and convergence was assumed when both the energy and the charge difference between the last two iterations were less than 0.0001 Ry and 0.001*e*, respectively. Scalar relativistic corrections were added and spin–orbit coupling was incorporated using the second variational procedure [30].

3. Results and discussion

3.1. Synthesis

$YbNi_{2-x}Fe_xAl_8$ was isolated from the reaction of Yb, Ni, and Fe in excess liquid aluminum. When equal amount of Ni and Fe was used, the fraction of $YbNi_{2-x}Fe_xAl_8$ was as high as 70%; however ~20% of $Yb_3Ni_5Al_{19}$ was also isolated as a side product. Interestingly, attempts to grow larger single crystals of $YbNi_{2-x}Fe_xAl_8$ by scaling up the reaction resulted in much improved fraction (~90%) while the crystals sizes remained similar to those of the smaller scale reactions.

3.2. Crystal structure

$YbNi_{2-x}Fe_xAl_8$ crystallizes in the $CaCo_2Al_8$ structure type in the space group *Pbam*. This is a rather stable structural arrangement as a number of isotypical ternary phases have been reported as mentioned in the Introduction. $YbNi_{2-x}Fe_xAl_8$ seems to be the first quaternary analog of this structure type. In the unit cell, there is one crystallographically independent Yb site, two *M* sites (mixed occupied by Ni and Fe) and nine Al sites, see Table 2. The structure can be thought of as a stuffed three-dimensional aluminum framework. Fig. 2A depicts the structure with the Yb and transition metal atoms removed. The all aluminum framework features trigonal prismatic and pentagonal columns in which the transition metals and the Yb atoms, respectively, reside (Fig. 2B).

Fig. 3 depicts the structure of $YbNi_{2-x}Fe_xAl_8$ in polyhedral representation, viewed down the *c*-axis. The *M*(1)- and *M*(2)-centered polyhedra, composed of Al atoms, form a three-dimensional framework with Yb ions sitting in small channels. Each channel is composed of two *M*(1)-polyhedra and three *M*(2)-polyhedra which connect with each other by sharing Al corners. As is shown in Fig. 4, the coordination environments of *M*(1) and *M*(2) atoms are similar and best described as tri-capped trigonal prisms composed of Al atoms. On the *ab* plane, the *M*(1) polyhedra are condensed into dimers by sharing faces containing

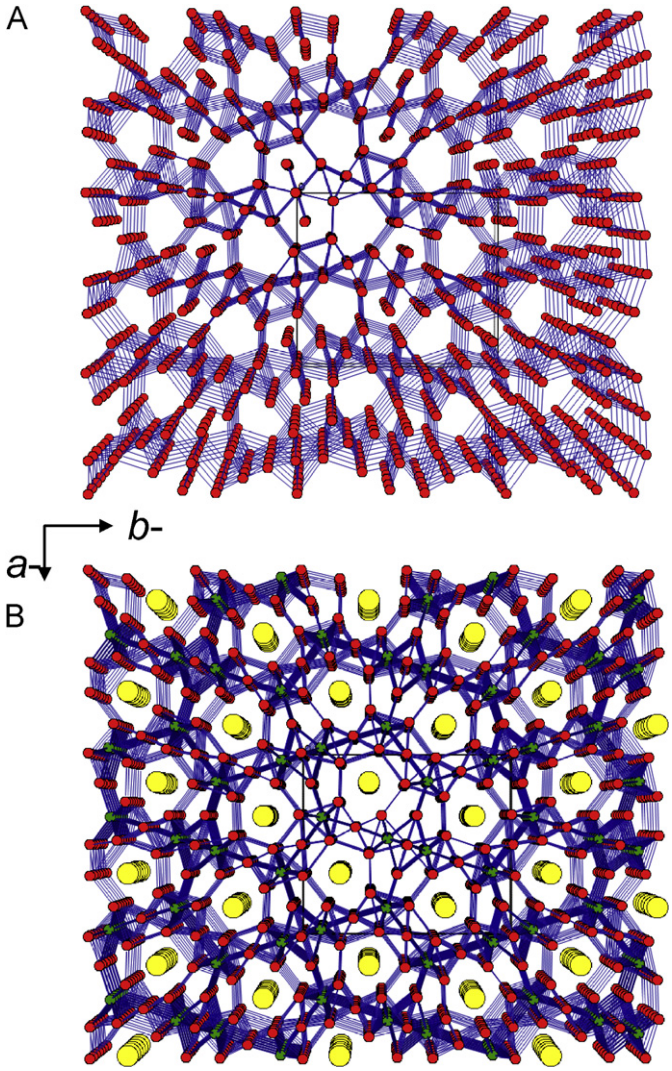

Fig. 2. (A) The aluminum only framework in $YbNi_{2-x}Fe_xAl_8$ and (B) the same framework with Yb and $M(1)/M(2)$ atoms added (M = Ni, Fe).

two Al(1) and Al(9) atoms. The bond distance between $M(1)$ atoms is 2.5069(16) Å. Along the c direction, these $M(1)$-centered polyhedra share Al triangular faces defined by the Al(1), Al(2) and Al(7) atoms. The distances between these Al atoms range from 2.6165(12) to 2.998(2) Å, see Table 3. The coordination geometry of the $M(2)$ atom resembles that of $M(1)$: each $M(2)$ atom is surrounded by nine Al atoms which form a tri-capped trigonal prism. Along the c-axis, these trigonal prisms share the Al-based trigonal faces but without forming $M(2)$ dimers on the ab plane.

The Yb atoms reside in distorted pentagonal prisms composed of Al atoms. The prisms are penta-capped and form an infinite column as mentioned above. This geometry is similar to those of the Yb atoms in $Yb_3Ni_5Al_{19}$, which are also in distorted coordination environment [19]. The distance from Yb to Al(9) is very long at 3.412(3) Å, while those to the other Al neighbors vary from 3.0717(18) to 3.359(2) Å, see Table 4.

3.3. Physical properties

Because of the explicit needle-like morphology and the relatively large crystal size of $YbNi_{2-x}Fe_xAl_8$, we were able to study its magnetic properties both isotropically (polycrystalline) and anisotropically (single crystal). The temperature-dependent

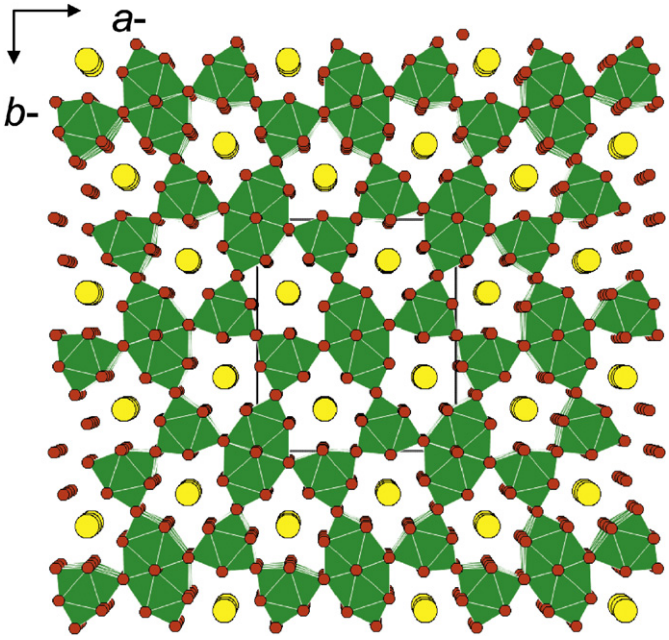

Fig. 3. Crystal structure of $YbNi_{2-x}Fe_xAl_8$ in polyhedral representation based on $M(1)$ and $M(2)$ atoms polyhedra. View down the [001] direction.

molar magnetic susceptibility data conducted on a polycrystalline sample is shown in Fig. 5A. Above 50 K, the inverse magnetic susceptibility data follows Curie–Weiss Law, with calculated $\mu_{eff} = 2.19\,\mu_B$, which is between the theoretical value for Yb^{2+} ($0\,\mu_B$) and Yb^{3+} ($4.54\,\mu_B$) ions assuming Hund's rule. There is no evidence that the Fe atoms carry any magnetic moments in this compound and this is consistent with the results of the calculations described below. The lower μ_{eff} value than that expected for Yb^{3+} may be attributed to several factors, one being mixed valency. This issue is addressed in the theoretical calculations section discussed later. Other possible origins of the reduced moment at high temperatures can be either crystal field effects or exchange interaction between the f^{13} moments and conduction electron spins.

The observed reduced moment suggests that the Yb ions in this compound are of mixed-valent nature. However, no broad hump was observed in the T-dependence of the susceptibility which is typical of mixed-valent systems [31]. Similar magnetic behavior was observed in the Kondo-lattice compound $Yb_2Ir_3Ge_5$. We will provide an alternate explanation for the reduced moment based on the results of electronic structure calculations. The negative value of the Weiss constant ($\theta = -92.2$ K) implies strong coupling between the f^{13}-states and the conduction band, however, no magnetic ordering was observed down to 3 K. Below 20 K, the inverse magnetic susceptibility changes slope, probably due to thermal depopulation arising from crystal field effects and changes in valence configuration.

The magnetization behavior of $YbNi_{2-x}Fe_xAl_8$ with the applied field perpendicular and parallel to the c-axis is shown in Fig. 5B. Substantial magnetic anisotropy was observed and in both orientations there was no sign of magnetic saturation up to 55,000 G. When the field is perpendicular to the c-axis, the magnetization values are higher than when it is parallel. This orientation-dependent behavior suggests that it is easy to orient the magnetic moment in the ab plane—i.e. it is an easy plane system. When the field is perpendicular to the c-axis, the magnetization corresponds to $0.16\,\mu_B$ at 55,000 G, which is only about 4% of the saturation value. Here is it worth mentioning that the related gallide compound $YbCo_2Ga_8$ remains diamagnetic

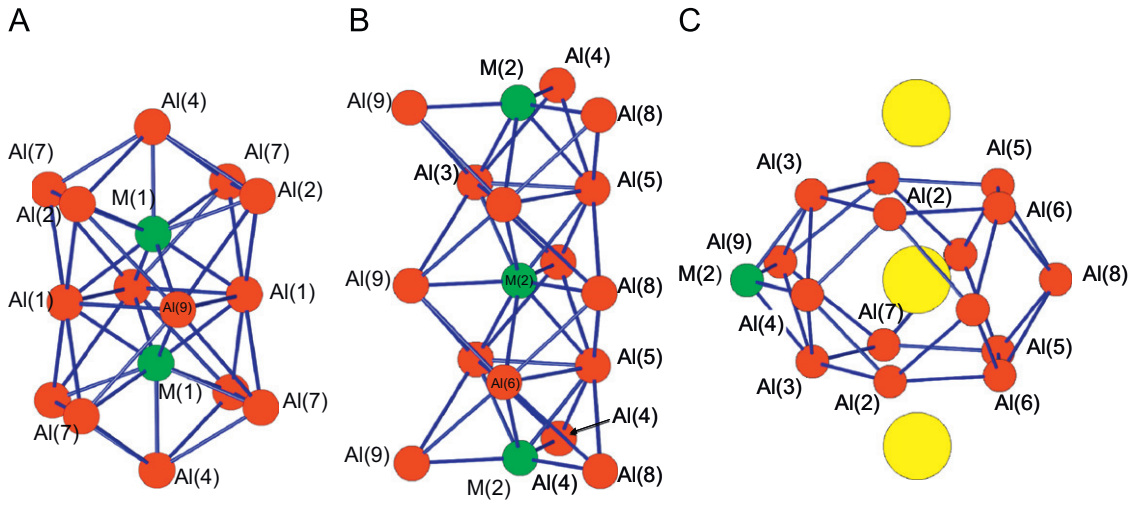

Fig. 4. Coordination environments of (A) *M*(1) atoms (green), (B) *M*(2) atoms (green) and (C) Yb atoms (yellow). Aluminum atoms are shown in red.

Table 3
Selected bond lengths (Å) in $YbNi_{2-x}Fe_xAl_8$ with estimated standard deviations

Bond	Distance	Bond	Distance
Yb–Al(2) × 2	3.3546(18)	*M*(2)–Al(6)	2.4053(13)
Yb–Al(3) × 2	3.0854(17)	*M*(2)–Al(9)	2.744(2)
Yb–Al(5) × 2	3.359(2)	Al(1)–Al(5) × 4	2.6165(12)
Yb–Al(6) × 2	2.9283(16)	Al(2)–Al(4) × 2	2.6898(18)
Yb–Al(7) × 2	3.0717(18)	Al(2)–Al(6)	2.821(4)
Yb–Al(8)	3.2717(3)	Al(3)–Al(4) × 2	2.998(2)
M(1)–Al(2) × 2	2.7455(17)	Al(3)–Al(9) × 2	2.948(2)
M(1)–Al(7) × 2	2.5693(16)	Al(4)–Al(5) × 2	2.7135(18)
M(1)–Al(9) × 2	2.528(2)	Al(4)–Al(7) × 2	2.8470(14)
M(1)–*M*(1)	2.5069(16)	Al(5)–Al(6)	2.725(3)
M(2)–Al(3) × 2	2.5344(16)	Al(5)–Al(7)	2.8349(19)
M(2)–Al(5)	2.7367(18)		

Table 4
^{57}Fe Mössbauer spectral parameters for $YbNi_{2-x}Fe_xAl_8$ at room temperature and 80 K

Temperature (K)	Site *M*(1)			Site *M*(2)		
	IS_{Fe} (mm/s)	ΔE_q (mm/s)	Area (%)	IS_{Fe} (mm/s)	ΔE_q (mm/s)	Area (%)
300	0.15(2)	0.63(2)	67(2)	0.28(2)	0.37(2)	33(2)
80	0.25(2)	0.63(2)	66(2)	0.42(2)	0.41(2)	34(2)

down to lowest temperatures apparently containing only Yb^{2+} species [32].

Fig. 6A illustrates the temperature-dependent electrical resistivity $\rho(T)$, which shows metallic character of $YbNi_{2-x}Fe_xAl_8$. The resistivity value at room temperature is ~120 μΩ cm; it drops with decreasing temperature, saturating to a constant value at lower temperatures. At $T<50$ K the temperature dependence is similar to that seen in $Yb_2Ir_3Ge_5$ [31], more like that of a Kondo-lattice system. The thermoelectric power is very small at around −1 μV/K at room temperature, confirming the strong metallic character of $YbNi_{2-x}Fe_xAl_8$.

To probe the electronic state of Fe in $YbNi_{2-x}Fe_xAl_8$, the ^{57}Fe Mössbauer spectra were taken at 80 K and room temperature. The spectra were fitted with Lorentzian form, shown in Fig. 7. The Mössbauer spectral parameters are listed in Table 4.

The spectrum consists of two doublets that reflect the two Fe atomic sites (*M*(1) and *M*(2)) in the structure. The doublet with

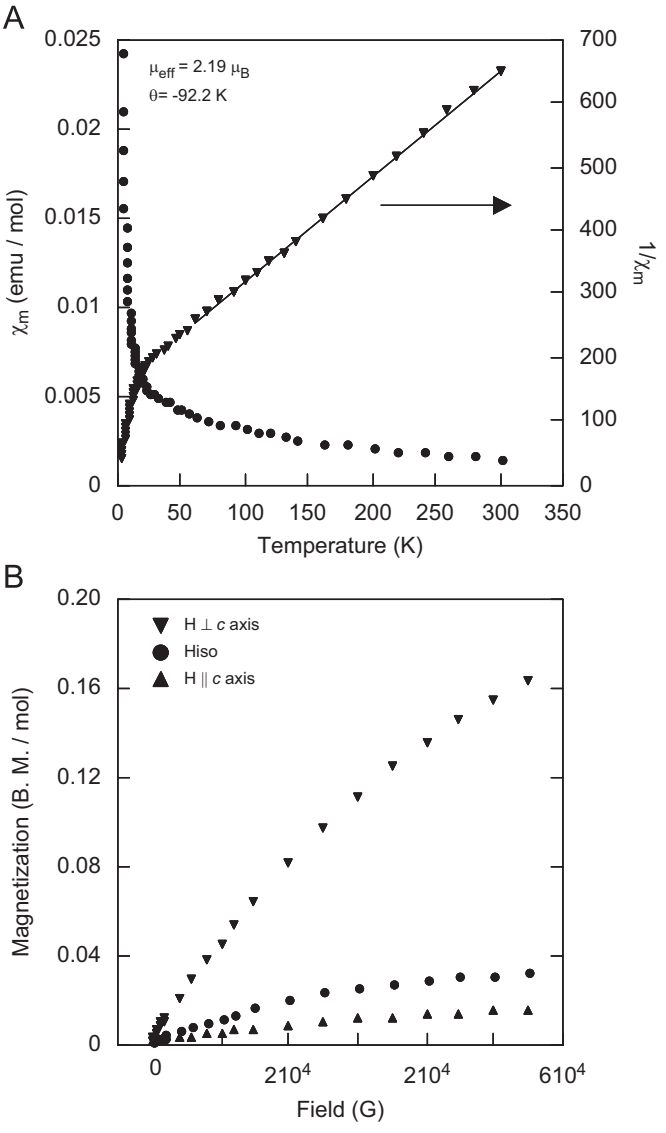

Fig. 5. (A) Temperature-dependent magnetic susceptibility of a polycrystalline sample of $YbNi_{2-x}Fe_xAl_8$ under the applied field of 1000 G. (B) Molar magnetization of $YbNi_{2-x}Fe_xAl_8$ single crystals oriented with [001] axis perpendicular and parallel to the external magnetic field, and randomly in fields up to 55,000 G.

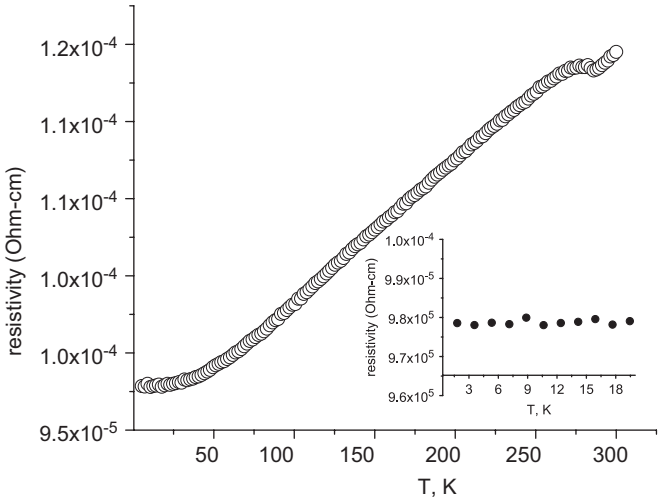

Fig. 6. Temperature-dependent electrical resistivity for a polycrystalline pellet of $YbNi_{2-x}Fe_xAl_8$. The small kink in the data at ~280 K is believed to be an experimental artifact.

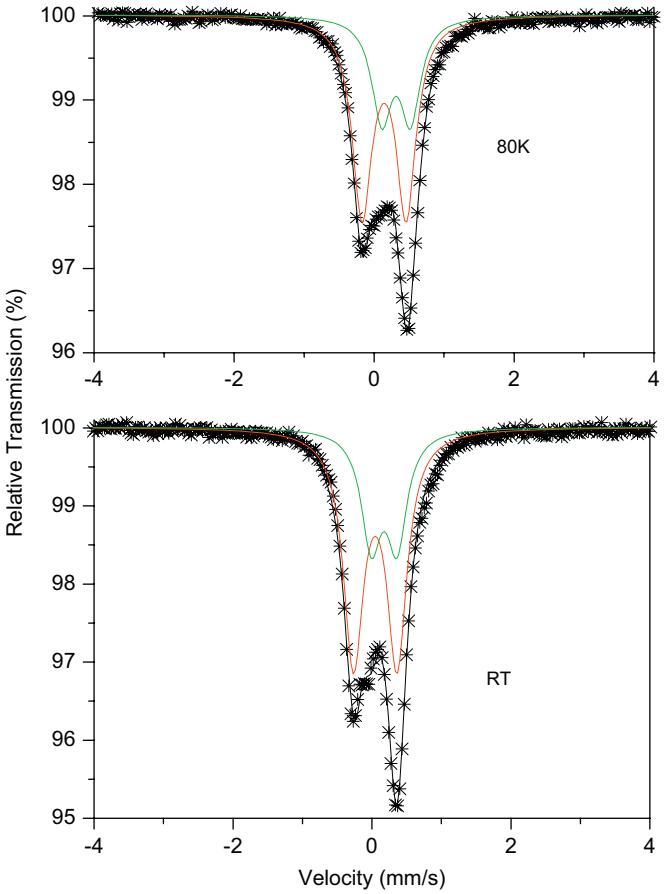

Fig. 7. ^{57}Fe Mössbauer spectra of $YbNi_{2-x}Fe_xAl_8$ at 80 K and RT. The green and red lines are the relative contributions from sites $M(1)$ and $M(2)$ obtained from spectral deconvolution.

large quadrupole splitting is assigned to site Fe(1) while that with the smaller quadrupole value is attributed to site Fe(2). This assignment is based on the fact that Fe(1) is bonded to another Fe(1) atom in addition to nine Al atoms, Fig. 4A, resulting in a larger principal electric field gradient than that of Fe(2). For the Fe(1) site, the quadrupole splitting values ΔE_q are the same at RT and at 80 K at 0.63(2) mm/s. For the Fe(2) site, the ΔE_q values are 0.37(2) and 0.41(2) mm/s at RT and 80 K, respectively. The similarities of the quadrupole splitting values (ΔE_q) at different temperatures confirm the absence of any phase transition in this temperature range. In addition, the isomer shift of Fe(1) is 0.25(2) mm/s at 80 K, very close to the values of metallic Fe; however the isomer shift of Fe(2) is much higher at 0.42(2) mm/s which is more indicative of a ferric character. We observed no evidence of any magnetic ordering residing on the Fe atom sites. This type of nonmagnetic character of the Fe atoms was also observed in other Fe-containing intermetallic compounds, such as $REFe_2Al_{10}$ [33], $RE_2Fe_3Si_5$ [34], $RE_4Fe_{2+x}Al_{7-x}Si_8$ [35] and $RE_4FeGa_{12-x}Ge_x$ [36]. The reasons for this are discussed below in the electronic structure calculations section.

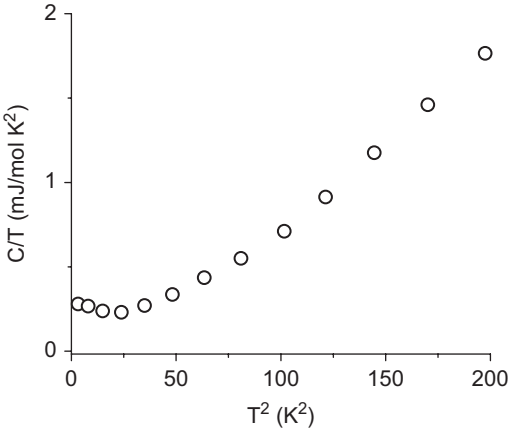

Fig. 8. Plot of C_p/T vs. T^2 of the heat capacity data for a sample of $YbNi_{2-x}Fe_xAl_8$.

Heat capacity data were collected and analyzed using the Debye low-temperature approximation given by

$$C_p = \gamma T + \beta T^3$$

where γ and β are the electron and phonon contributions to the total heat capacity, respectively [37]. As shown in Fig. 8, a linear region is obtained in the plot of $C(T)/T$ vs. T^2 below 20 K down to 10 K with a small electronic coefficient, γ, on the order of 1 mJ/mol K^2, typical of metals. A minimum in $C(T)/T$ is observed around 5 K with a slight upturn at lower temperatures suggesting an increase in density of states. A sharper upturn may exist at even lower temperatures; however, there is not strong evidence for heavy fermion behavior in $YbNi_{2-x}Fe_xAl_8$ above 1.8 K.

3.4. Electronic structure

Electronic structure calculations were performed in order to understand the nature of bonding between different atoms and the orbital distributions of Yb f-electrons as well as Ni and Fe d-electrons. According to the single-crystal structure refinement, the transition metal sites $M(1)$ and $M(2)$ are occupied by a mixture of Ni/Fe: 63%/37% on $M(1)$ and 46%/54% on $M(2)$. To model this mixed occupancy we constructed a $1\times1\times2$ supercell, which corresponds to placing two unit cells next to each other along the [001] direction. In one unit cell the $M(1)$ and $M(2)$ sites were assigned as Ni and Fe, respectively, while in the second unit cell the assignments were switched, i.e. Fe on $M(1)$ and Ni on $M(2)$. This supercell model corresponds to 50%/50% occupancy of Ni/Fe on both $M(1)$ and $M(2)$ sites, which is close to the experimental observation. The total number of atoms in the supercell is 88 (8 Yb, 8 Ni, 8 Fe and 64 Al atoms).

Before discussing the results of our calculations we make a few general remarks about the ability of LSDA+U calculations to

describe the physics of Yb (f^{14} and f^{13}) systems, particularly the mixed-valence ground state. There are many calculations which give the Yb^{3+} (f^{13})-state properly [38,39]. In these calculations 13*f*-states lie below the Fermi level (E_F) and 1*f*-state lies above E_F, the splitting between the occupied and unoccupied levels being $\sim U_{eff}$. The calculations by Antonov et al. for $YbInCu_4$ using the LMTO method indicate that the above single *f*-level is pinned to the Fermi energy thereby giving a mixed-valent ground state for this compound, which is in agreement with experiment. This pinning was found to be not very sensitive to the exact value of U_{eff} as long as it was >5 eV, but depend sensitively on the density of states associated with non-*f*-states. We have redone the calculation in this compound using all-electron FP-LAPW method and found the same result. Thus we conclude that LSDA+*U* calculation is capable of giving a mixed-valent ground state.

The total densities of spin-up and spin-down states for $YbNi_{2-x}Fe_xAl_8$ are shown in Figs. 9A and B, respectively. The main features of these two density-of-state (DOS) figures are the sharp peaks located between -5 and -7 eV below E_F, which is set to be at 0 eV. They are split by the anisotropy of the Coulomb interaction within the 4*f* shell of the Yb ions and the spin–orbit interaction. The peak (width $\sim$0.2 eV) located nearly 2 eV above the E_F, which is only present in Fig. 9A, represents the main difference between the spin-up and spin-down DOS. This band originates from the hole in the 4*f* spin-up state of Yb with $m_l = +2$ character. Convergent solutions were also obtained for unoccupied $|3\uparrow\rangle$, $|1\uparrow\rangle$ and $|0\uparrow\rangle$ states, but it was found that the lowest energy configuration corresponded to the case when the $|2\uparrow\rangle$ states were empty. Hund's rule state would correspond to unoccupied $|3\uparrow\rangle$ orbital. Despite the fact that LDA+*U*, for fixed *U*, is a variational method [40], the total energy criterion may sometimes lead to unphysical results. The reason for this is that different electronic configurations for which convergent solutions are obtained may require different *U* values. Therefore the "fixed *U*" may not lead to the real ground state configuration. However, the only difference between the one, which gives the lowest energy, and the other solution is their magnetic moments. This point will be discussed later.

The splitting within the *f* shell can be seen more clearly in Figs. 9C and D, which show the projected DOS of Yb 4*f*-states. The left panel (Fig. 9C) displays the spin-up DOS, with six out of seven states fully occupied, while the seventh spin-up state, located at 2 eV above E_F, is empty. In Fig. 9D, all seven 4*f* spin-down states are situated below E_F. From this picture we can conclude that the valence state of Yb is trivalent.

Another character shown in both total spin-up and spin-down DOS Figs. 9A and B is the uniform background due to Al, Ni and Fe states, as well as a finite DOS at the Fermi level, indicating the

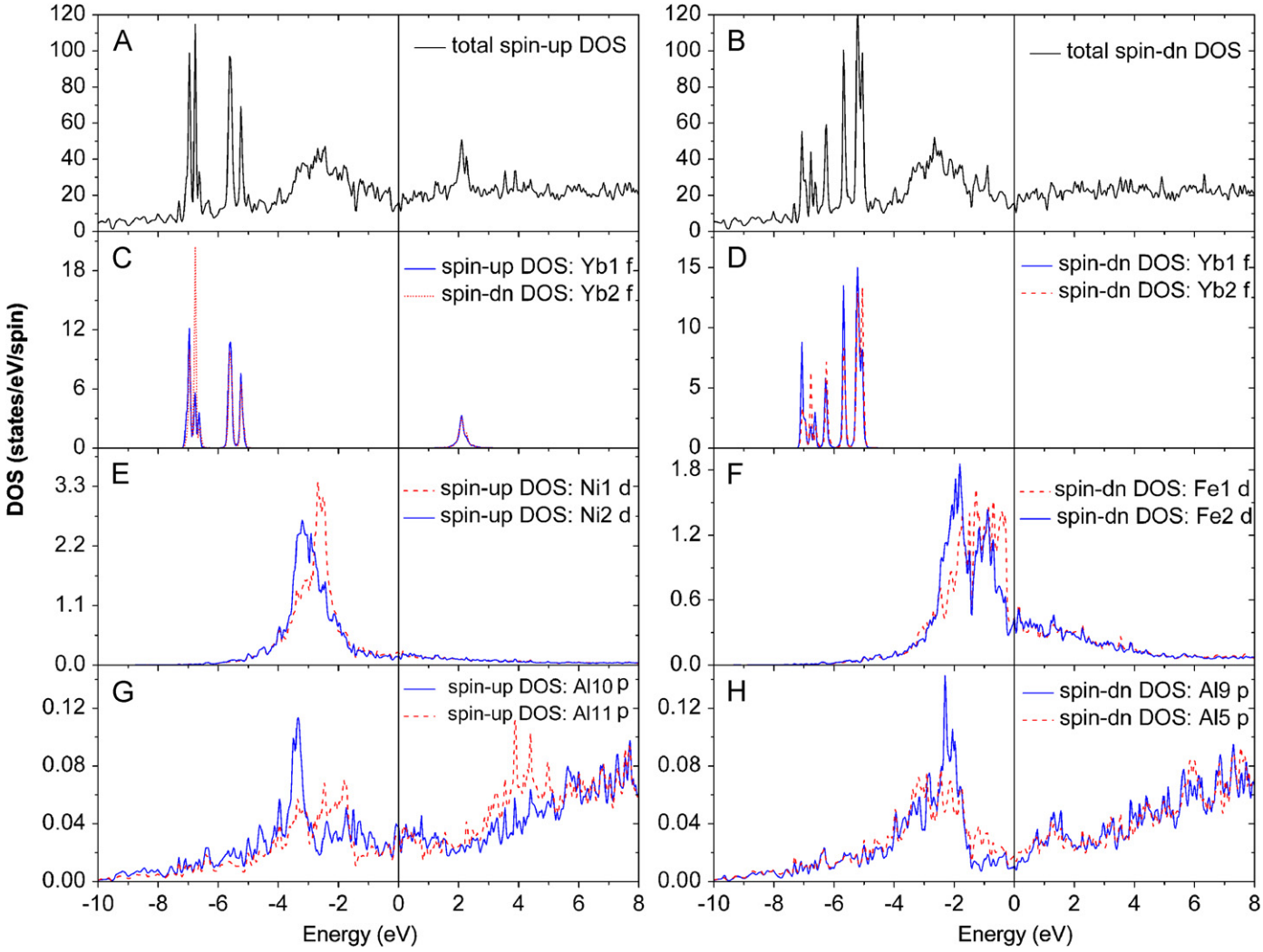

Fig. 9. Results from the electronic band calculations for $YbNi_{2-x}Fe_xAl_8$. (A and B) Total spin-up and spin-down DOS of $YbNi_{2-x}Fe_xAl_8$. (C) Yb 4*f* spin-up DOS, with six occupied states and one hole located at 2 eV. (D) Yb 4*f* spin-down DOS, with all seven states occupied. (E) Ni(1) 3*d* and Ni(2) 3*d* DOS. (F) Fe(1) 3*d* and Fe(2) 3*d* DOS. (G and H) *p*-States of Al atoms located around *M*(1) (Al(10) and Al(9)) and located around *M*(2) (Al(11) and Al(5)).

metallic nature of the system. This is consistent with very small value of thermopower observed in this system ($\sim -1\,\mu V/K$ at RT). The broad hump in the DOS located between E_F and -4 eV comes from the *d*-states of Ni and Fe. The Ni 3*d* bands (Fig. 9E) are located well below the E_F, suggesting a filled $3d^{10}$ configuration. Therefore, Ni is essentially reduced to a diamagnetic state ($d^8s^2 \rightarrow d^{10}$). This is also evident from the spin-up and spin-down DOS, which are almost identical for both Ni atoms. This type of behavior in late transition metals has been observed in several intermetallic systems containing more electropositive elements [41]. The Fe 3*d* spin-up states, shown in Fig. 9F, have a significant contribution to the DOS near the Fermi level, indicating that these states are not fully occupied. However, the spin-up and spin-down DOS of the Fe *d*-levels are identical, just as they were in the case of Ni. Thus Ni and Fe will lack a local magnetic moment and contribute only to Pauli paramagnetic susceptibility.

An interesting feature, shared by both Ni and Fe *d*-states, can be observed from Figs. 9E and F: they become energetically more stable when the atom occupies the *M*(2) site. The difference in the DOS of the *d*-levels of the Fe occupying different sites in the supercell is in agreement with the result of the Mössbauer spectroscopy which shows different local charge densities at two different Fe sites in the structure. The coordination environments of *M*(1) and *M*(2) sites are similar in that both are surrounded by 9 Al atoms, but in addition the transition metal atoms located at *M*(1) site form dimers. It seems that the dimer geometry reduces the degree of mixing between some Al *p*- and Ni/Fe *d*-orbitals. This can be verified by analyzing the contribution to the DOS of the *p*-orbitals of several different Al atoms. Figs. 9G and H show the *p*-states of Al(10) and Al(9) from the tri-capped trigonal prism surrounding *M*(2) as well as the *p*-states of Al(11) and Al(5) surrounding *M*(1). (The labeling of the Al atoms is different than that obtained from the crystallographic refinement, because the calculation was performed on a supercell.) It is evident that the Al *p*-states hybridize more with the *d*-states of Ni(2) and Fe(2) than with the *d*-states of Ni(1) and Fe(1). Probably, because of the higher degree of *p*–*d* hybridization between Al and Ni/Fe located on *M*(2), these states are energetically better stabilized.

Next we discuss the magnetic properties of the system coming primarily from the unfilled Yb *f*-shell. The calculated spin and orbital magnetic moments for the two Yb ions are: $\mu_{spin} = 1.0059\,\mu_B$; $\mu_{orb} = 1.9811\,\mu_B$ for Yb1 and $\mu_{spin} = 1.0044\,\mu_B$; $\mu_{orb} = 1.9810\,\mu_B$ for Yb2, which adds up to approximately $2.99\,\mu_B$ for both Yb ions suggesting a strong atomic character, trivalent configuration, and non-Hund's rule behavior. The fact that the 13 occupied and the 1 empty *f*-states are far removed from the Fermi energy argues against a mixed-valence picture. A similar result showing a hole in the 4*f* shell of Yb was recently obtained on $YbRh_2Si_2$ [38].

We have to mention that this kind of electronic structure, where the empty and occupied *f*-states are well separated and located far from E_F, together with the absence of long range magnetic order, suggests the possibility of Kondo-lattice scenario. We have to emphasize, however, that DFT with LSDA+*U* approximation is an effective single-particle theory and therefore cannot describe the complex correlated many-body ground state of a Kondo-lattice system.

4. Concluding remarks

The aluminide $YbNi_{2-x}Fe_xAl_8$ is the first quaternary analog of the $CaCo_2Al_8$ structure type and can crystallize from excess liquid Al. A mixed Ni/Fe occupancy appears to be present on the two transition metal sites (*M*(1) and *M*(2)) in the structure. The studies of the magnetization behavior show that the *ab* plane is the easy plane on which the magnetic moments are confined. Both resistivity and thermopower measurements on $YbNi_{2-x}Fe_xAl_8$ point to a strongly metallic character. Temperature-dependent magnetic susceptibility and electronic structure calculations using the LSDA+*U* formalism suggest that in these systems the Yb atoms are most likely in the f^{13} configuration. All magnetism in the compound derives from Yb^{3+} species and not from the Ni or Fe atoms. ^{57}Fe Mössbauer spectroscopy confirms the absence of magnetic ordering in this material and confirms the fact that the Fe atoms do not have a local magnetic moment. Finally, the results presented here point to the need to investigate in more detail the parent compound $YbCo_2Al_8$ with respect to magnetism, the role of Co atoms and the electronic state of Yb.

Acknowledgments

Financial support from the Department of Energy (Grant DE-FG02-07ER46356) is gratefully acknowledged.

Auxiliary material: Further details of the crystal structure investigation may be obtained from the Fachinformationzentrum Karlsruhe, D-76344 Eggenstein-Leopoldshafen, Germany (Fax: +49 7247 808 666; E-mail: crysdata@fiz-karlsruhe.de) on quoting depository number CSD419553.

References

[1] O. Trovarelli, C. Geibel, B. Buschinger, R. Borth, S. Mederle, M. Grosche, G. Sparn, F. Steglich, O. Brosch, L. Donnevert, Phys. Rev. B: Condens. Matter Mater. Phys. 60 (1999) 1136–1143.
[2] D. Kaczorowski, B. Andraka, R. Pietri, T. Cichorek, V.I. Zaremba, Phys. Rev. B: Condens. Matter Mater. Phys. 61 (2000) 15255–15261.
[3] Y. Singh, S. Ramakrishnan, Phys. Rev. B: Condens. Matter Mater. Phys. 68 (2003), 054419/1–054419/5.
[4] Z. Fisk, M.B. Maple, J. Alloys Compds. 183 (1992) 303–311.
[5] E. Czech, G. Cordier, H. Schaefer, J. Less-Common Met. 95 (1983) 205–211.
[6] M.B. Manyako, T.I. Tanson, O.I. Bodak, R. Cerny, K. Yvon, Z. Kristallogr. 211 (1996) 216.
[7] M.D. Koterlin, B.S. Morokhivskii, R.V. Lapunova, O.M. Sichevich, Fiz. Tverd. Tela (Sankt-Peterburg) 31 (1989) 297–299.
[8] I. Tamura, T. Mizushima, Y. Isikawa, J. Sakurai, J. Magn. Magn. Mater. 220 (2000) 31–38.
[9] O. Tougait, D. Kaczorowski, H. Noel, J. Solid State Chem. 178 (2005) 3639–3647.
[10] O.M. Sichevits, R.V. Lapunova, Y.N. Grin, Y.P. Yarmolyuk, Izv. Akad. Nauk SSSR Met. (1985) 117–118.
[11] R.E. Gladyshevskii, Y.P. Yarmolyuk, Y.N. Grin, Kristallografiya 28 (1983) 1090–1093.
[12] M. Schlüter, W. Jeitschko, Inorg. Chem. 40 (2001) 6362–6368.
[13] R. Pottgen, D. Kubmann, Z. Anorg. Allg. Chem. 627 (2001) 55–60.
[14] M.G. Kanatzidis, R. Pottgen, W. Jeitschko, Angew. Chem. Int. Ed. 44 (2005) 6996–7023.
[15] P. Hohenberg, W. Kohn, Phys. Rev. B: Condens. Matter Mater. Phys. 136 (1964) B864.
[16] W. Kohn, L.J. Sham, Phys. Rev. 140 (1965) 1133.
[17] V.I. Anisimov, J. Zaanen, O.K. Andersen, Phys. Rev. B: Condens. Matter Mater. Phys. 44 (1991) 943–954.
[18] M.T. Czyzyk, G.A. Sawatzky, Phys. Rev. B: Condens. Matter Mater. Phys. 49 (1994) 14211–14228.
[19] E.D. Bauer, S. Bobev, J.D. Thompson, M.F. Hundley, J.L. Sarrao, A. Lobos, A.A. Aligia, J. Phys.: Condens. Matter 16 (2004) 4025–4032.
[20] SMART, fifth ed., Siemens Analytical X-ray Systems, Inc., Madison, WI, 1998.
[21] SAINT, fourth ed., Siemens Analytical X-ray Instruments, Inc., Madison, WI.
[22] G.M. Sheldrick, SADABS, University of Gottingen, Gottingen, Germany.
[23] G.M. Sheldrick, SHELXTL, Structure Determination Programs, 5.0 ed., Siemens Analytical X-ray Instruments, Inc., Madison, WI, 1995.
[24] D.D.C. Palmer, CrystalDiffract, 1995–1996.
[25] D. Singh, Planewaves, Pseudopotentials, and the LAPW Method, Kluwer Academic, Boston, MA, 1994.
[26] K. Schwarz (Ed.), WIEN2K, An Augmented Plane Wave+Local Orbitals Program for Calculating Crystal Properties, Wien, Austria, 2001.
[27] J.P. Perdew, Y. Wang, Phys. Rev. B 45 (1992) 13244–13249.
[28] J.F. Herbst, J. Wilkins, Handbook of Physics and Chemistry of Rare Earths, vol. 10, North-Holland, Amsterdam, p. 321.
[29] W.E. Pickett, S.C. Erwin, E.C. Ethridge, Phys. Rev. B: Condens. Matter Mater. Phys. 58 (1998) 1201–1209.
[30] A.H. MacDonald, W.E. Pickett, D.D. Koelling, J. Phys. C—Solid State Phys. 13 (1980) 2675–2683.
[31] B.C. Sales, D.K. Wohlleben, Phys. Rev. Lett. 35 (1975) 1240–1244.

[32] V. Fritsch, S. Bobev, N.O. Moreno, Z. Fisk, J.D. Thompson, J.L. Sarrao, Phys. Rev. B 70 (2004).
[33] V.M.T. Thiede, T. Ebel, W. Jeitschko, J. Mater. Chem. 8 (1998) 125–130.
[34] A.R. Moodenbaugh, D.E. Cox, C.B. Vining, C.U. Segre, Phys. Rev. B: Condens. Matter Mater. Phys. 29 (1984) 271–277.
[35] (a) B. Sieve, S. Sportouch, X.Z. Chen, J.A. Cowen, P. Brazis, C.R. Kannewurf, V. Papaefthymiou, M.G. Kanatzidis, Chem. Mater. 13 (2001) 273–283;
(b) B. Sieve, D.L. Gray, R. Henning, T. Bakas, A.J. Schultz, M.G. Kanatzidis, Chem. Mater. 20 (2008) 6107–6115.
[36] M.A. Zhuravleva, X. Wang, A.J. Schultz, T. Bakas, M.G. Kanatzidis, Inorg. Chem. 41 (2002) 6056–6061.
[37] C. Kittel, Introduction to Solid State Physics, Wiley, New York, 2005.
[38] G.A. Wigger, F. Baumberger, Z.X. Shen, Z.P. Yin, W.E. Pickett, S. Maquilon, Z. Fisk, Phys. Rev. B: Condens. Matter Mater. Phys. 76 (2007), 035106/1–035106/10.
[39] V.N. Antonov, M. Galli, F. Marabelli, A.N. Yaresko, A.Y. Perlov, E. Bauer, Phys. Rev. B 62 (2000) 1742–1752.
[40] A.B. Shick, A.I. Liechtenstein, W.E. Pickett, Phys. Rev. B: Condens. Matter Mater. Phys. 60 (1999) 10763–10769.
[41] G.V. Vajenine, R. Hoffmann, J. Am. Chem. Soc. 120 (1998) 4200–4208.